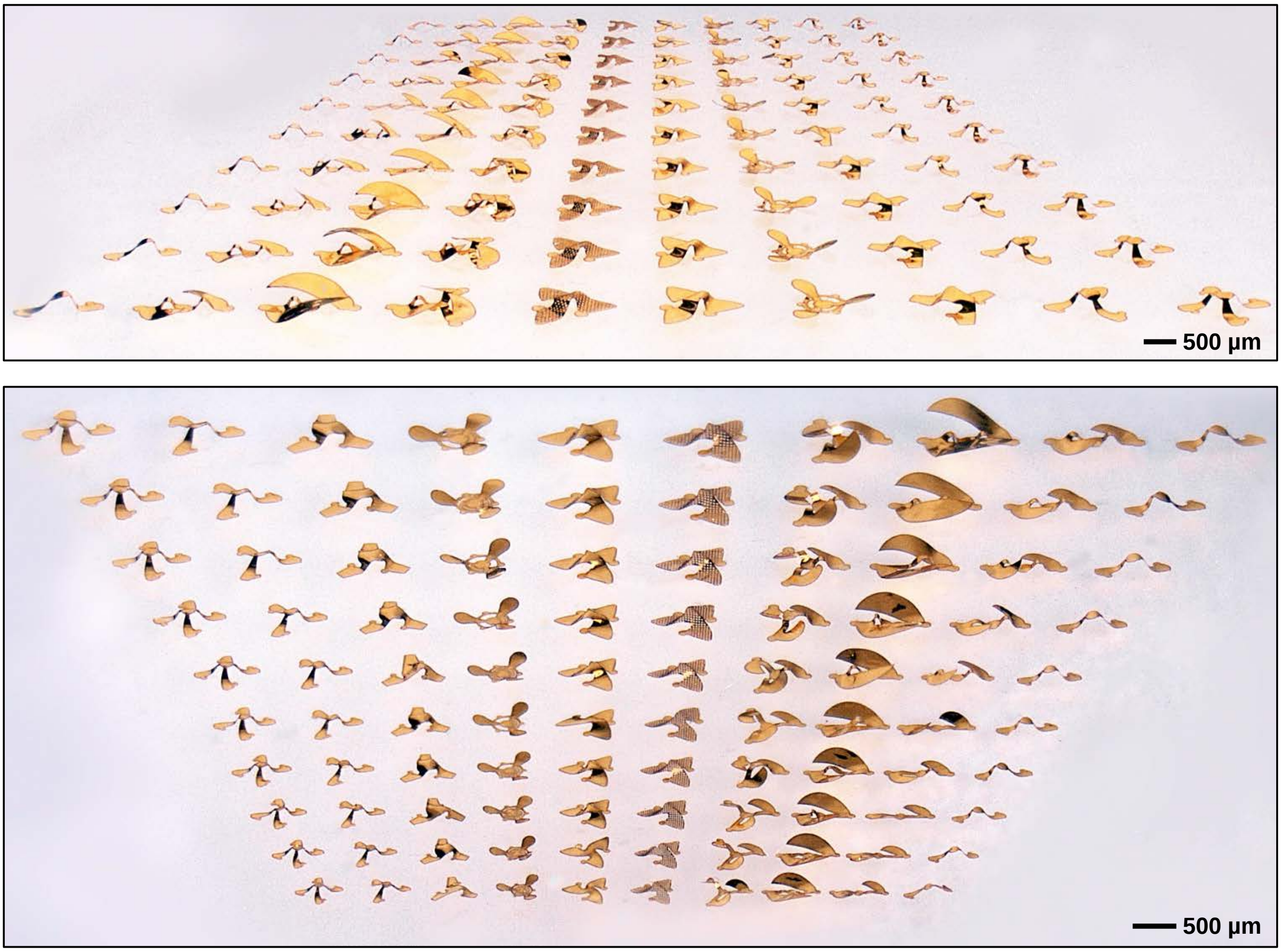

Figure S1. Bioinspired 3D micro-, and mesofliers. Photographs of a 10 x 10 array of 3D micro- and mesofliers.

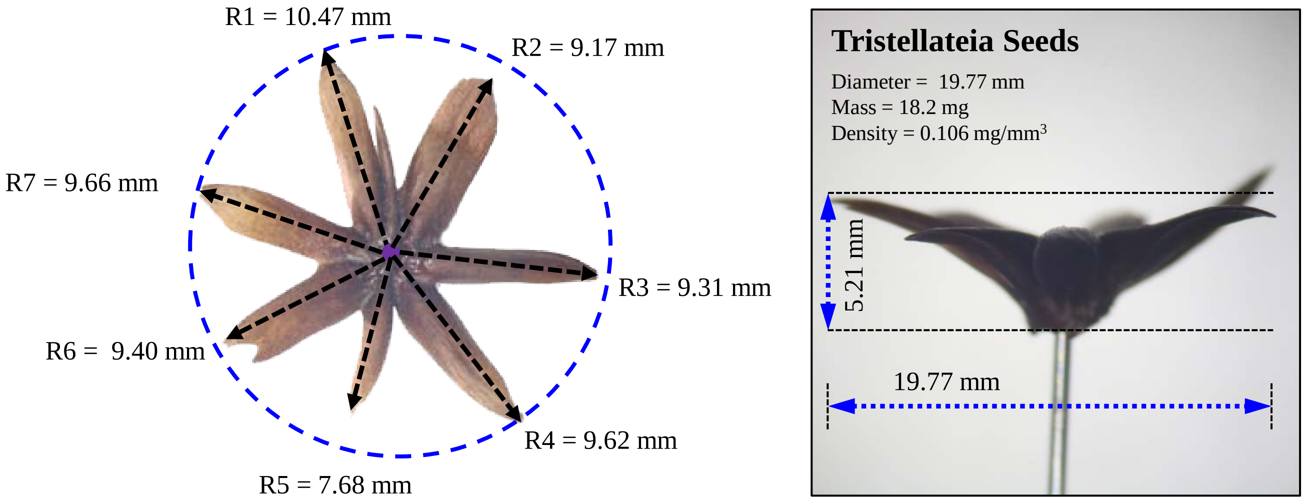

Figure S2. A tristellateia seed. Top-view and cross section view photographs of a tristellateia seed.

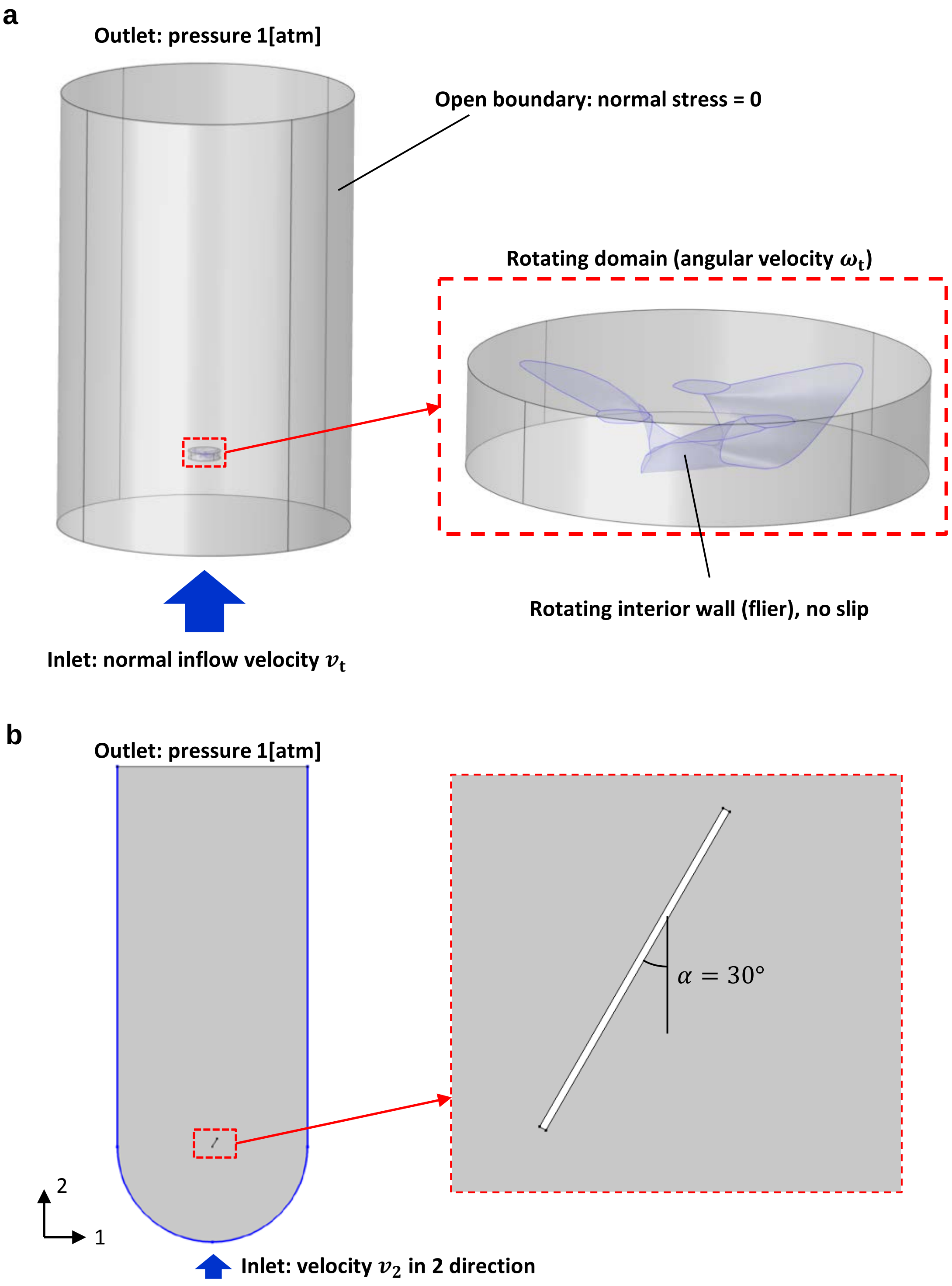

Figure S3. Schematic diagram of the configuration for Computational Fluid Dynamics Simulation. (a) 3D rotational falling fliers and (b) 2D airfoil.

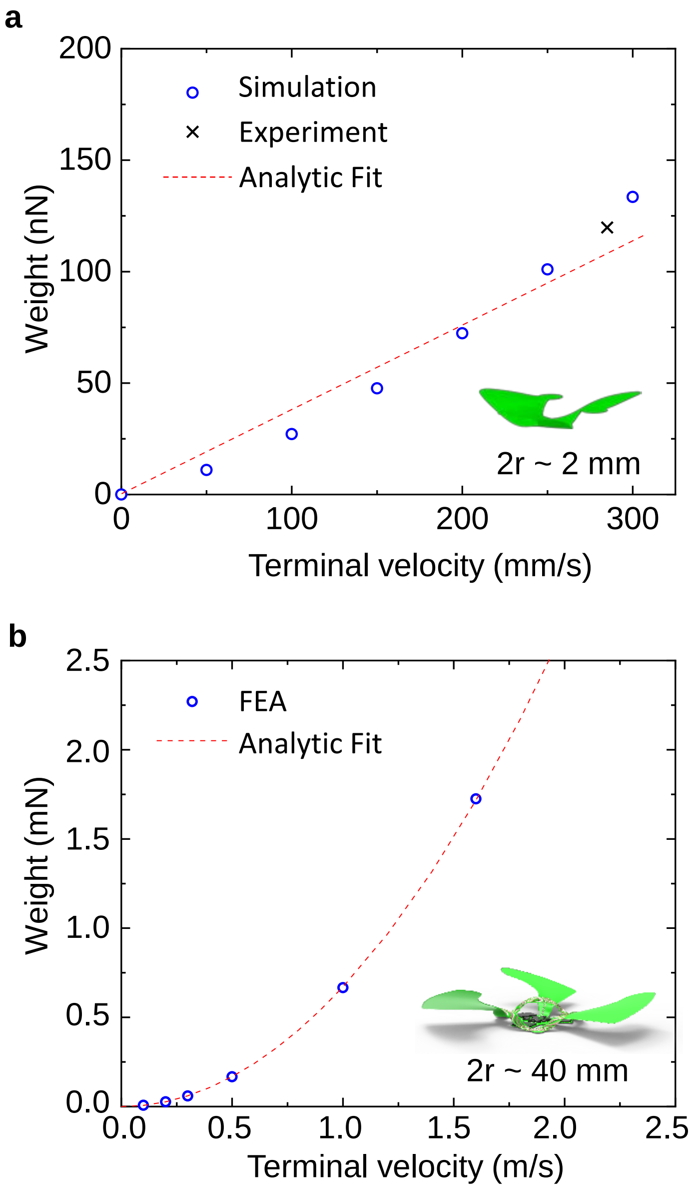

Figure S4. Relation between flier weight and terminal falling velocity. (a) Plot that indicates a nearly linear relationship between weight and terminal velocity for a mesoflier with small Reynolds number (Re~40). (b) Plot that indicates an approximately parabolic relationship between weight and terminal velocity for a macroflier with large Reynolds number (Re~3000).

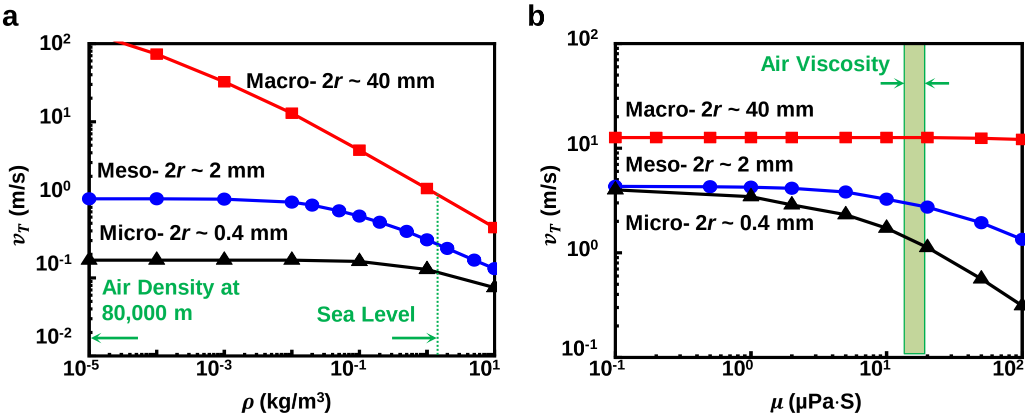

Figure S5. Effect of air properties. (a) Density and (b) Dynamic viscosity on the terminal velocity of multi-scale fliers.

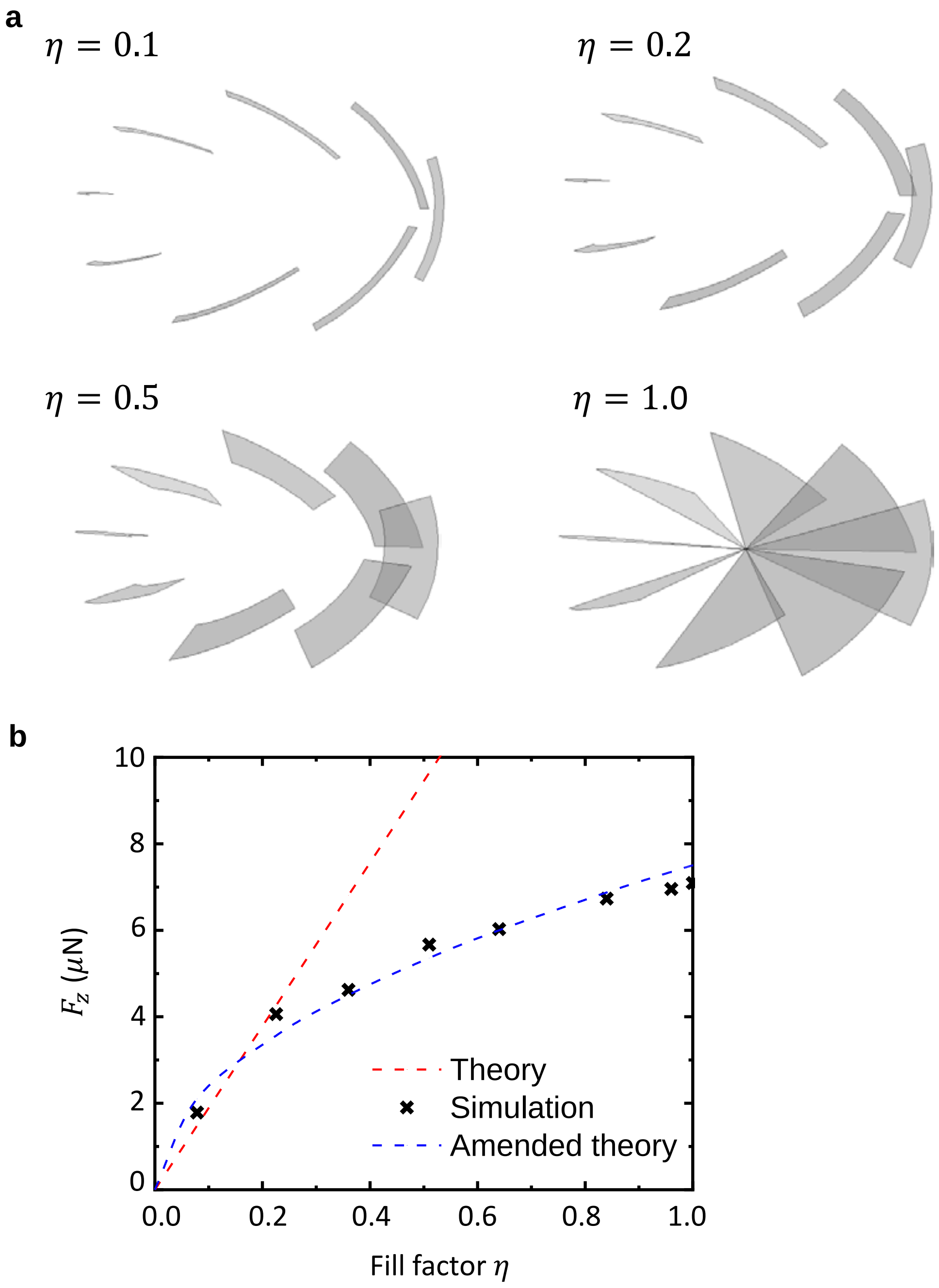

Figure S6. Amended dependence of the vertical-direction drag force of a 3D mesoflier on the fill factor at small Reynolds number (Re~40). (a) Schematic diagram of the simplified mesoflier model with various fill factors. (b) Weight to terminal velocity ratio versus fill factor for a mesoflier at small Reynolds number.

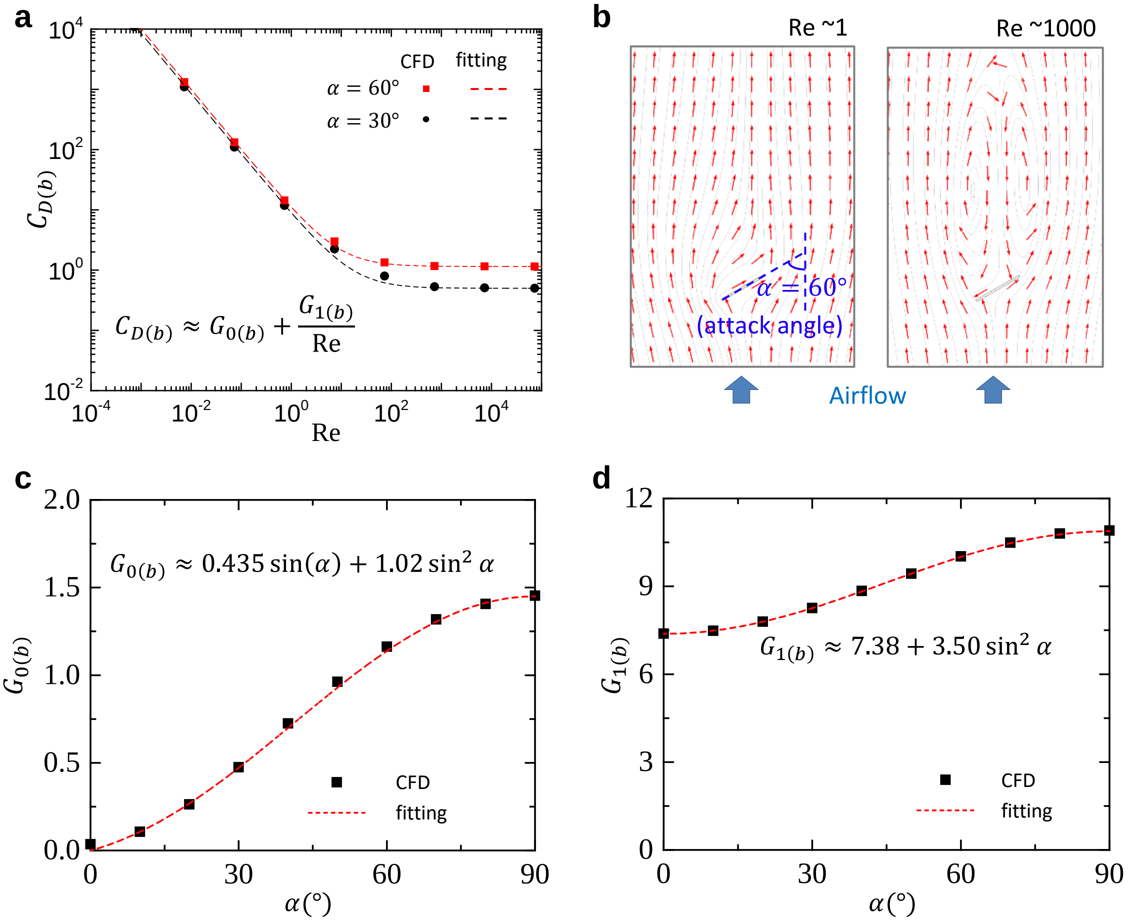

Figure S7. Aerodynamic properties of 2D flat airfoil (cross-section of blade) for various attack angles. (a) Drag coefficient of the 2D airfoil versus the Reynolds number. CFD results are fitted by $C_{D(b)} \approx G_{0(b)} + \frac{G_{1(b)}}{\mathrm{Re}}$, that $(G_{0(b)}, G_{1(b)}) = (0.50, 8.3)$ for $\alpha = 30°$ and $(G_{0(b)}, G_{1(b)}) = (1.15, 10)$ for $\alpha = 60°$. (b) Stream and quiver plot for the flow field around a flat airfoil of attack angle $\alpha = 60^o$, for Re ~ 1 and 1000, respectively. CFD results of (c) $G_{0(b)}$ and (d) $G_{1(b)}$ of the 2D airfoil versus the attack angle, as analytically fitted by $G_{0(b)} \approx 0.435\sin(\alpha) + 1.02\sin^2\alpha$ and $G_{1(b)} \approx 7.38 + 3.50\sin^2\alpha$, respectively.

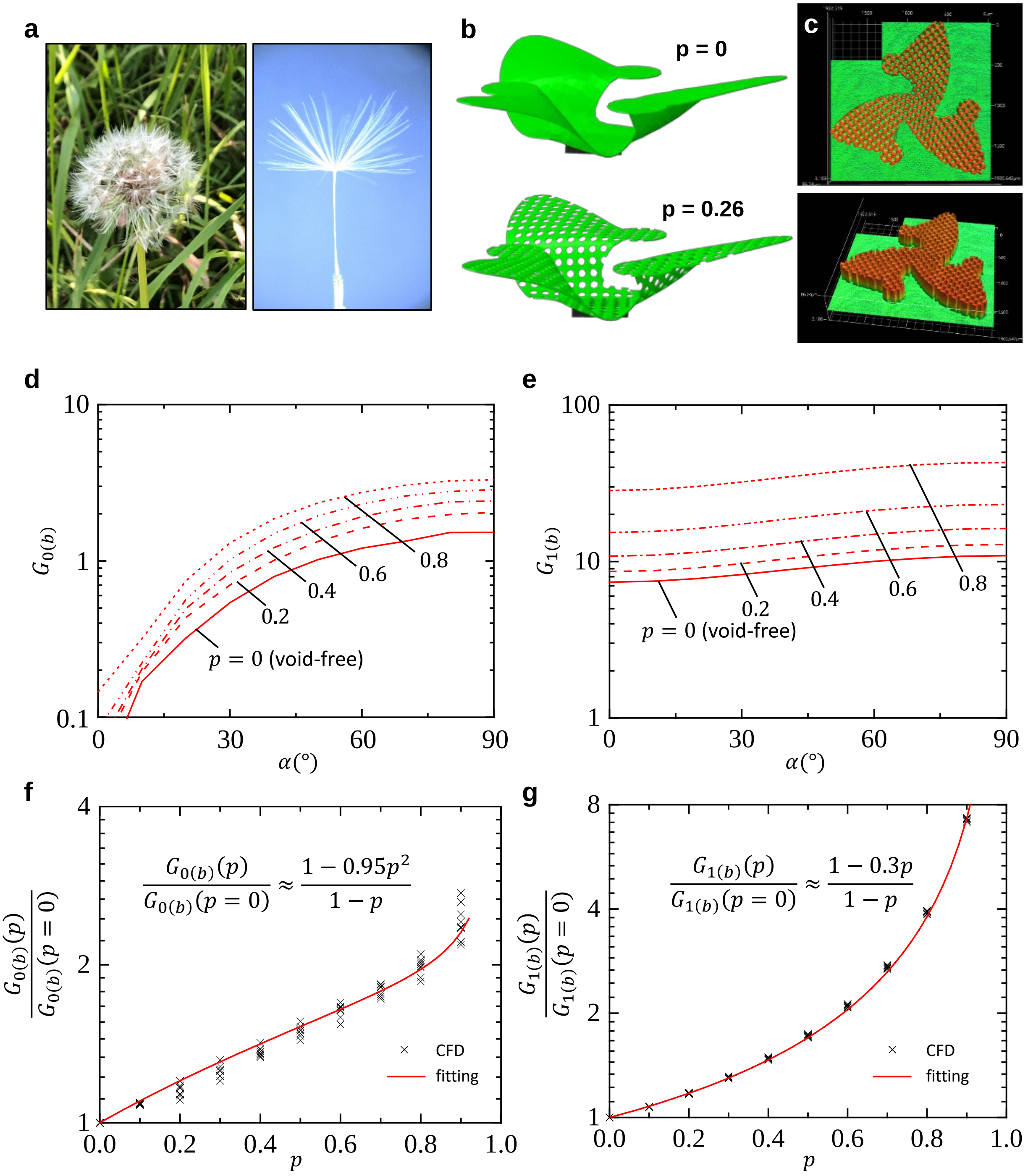

Figure S8. 3D microflier with porous design. (a) Inspiration of porosity from nature: optical images of Dandelion seeds and a feather. (b) FE simulated configuration of a 3D void-free microflier ($p = 0$) and a 3D microflier of porosity design ($p = 0.26$). (c) Images of scanned thickness of a 2D precursor for a porous microflier, with top view and perspective view, respectively. (d) $G_{0(b)}$ and (e) $G_{1(b)}$ versus the attack angle for various porosities. Normalized (f) $G_{0(b)}$and (g) $G_{1(b)}$ over their void-free values versus porosity, with the CFD values of various $\alpha \in [0°, 90°]$ and analytic fittings.

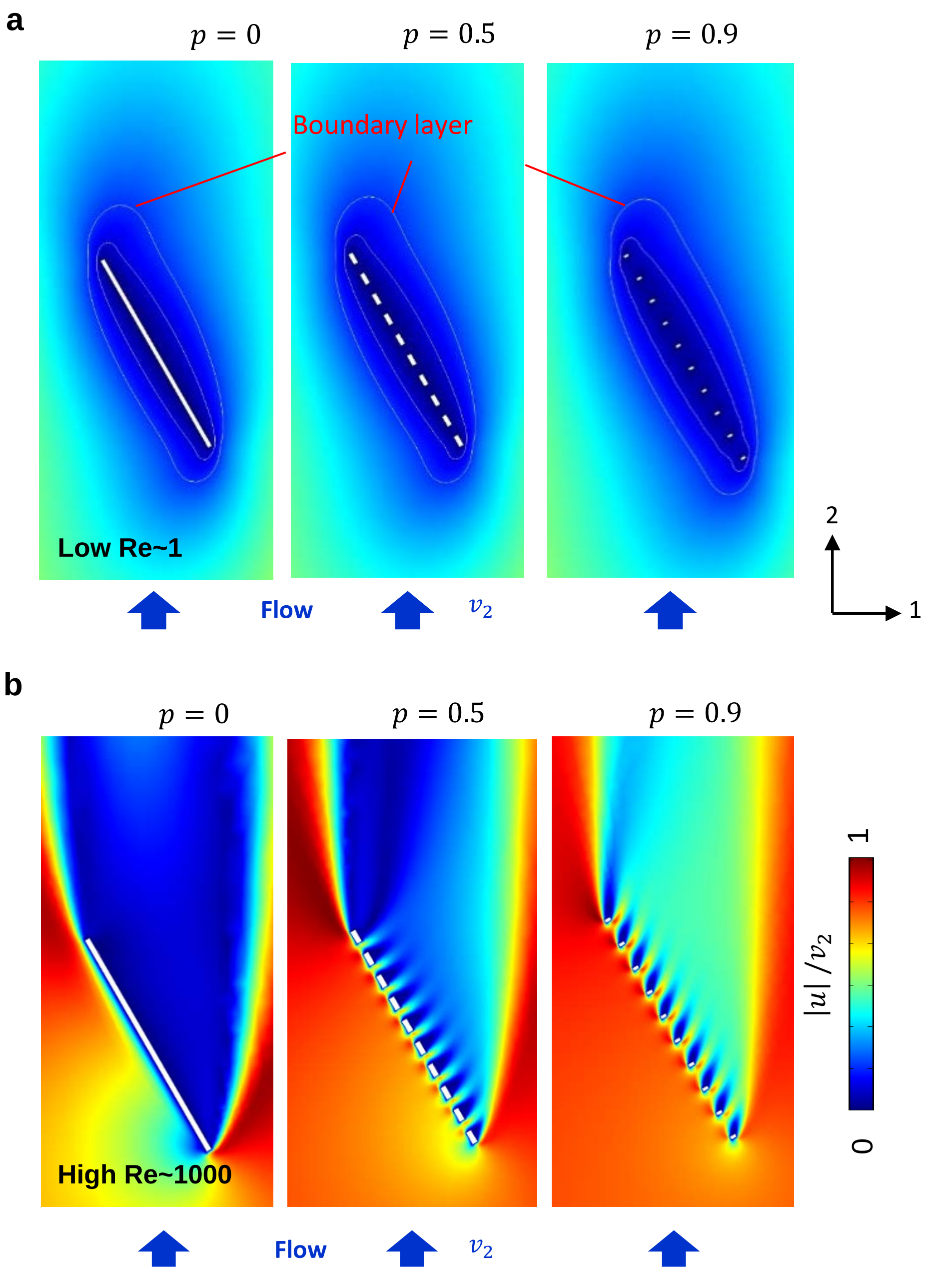

Figure S9. Velocity fields for airfoil with 3 different porosities (p=0, 0.5 and 0.9). (a) low Re and (b) high Re. The boundary layers at low Re are shown by velocity contours at $|u|/v_2 = 0.1$.

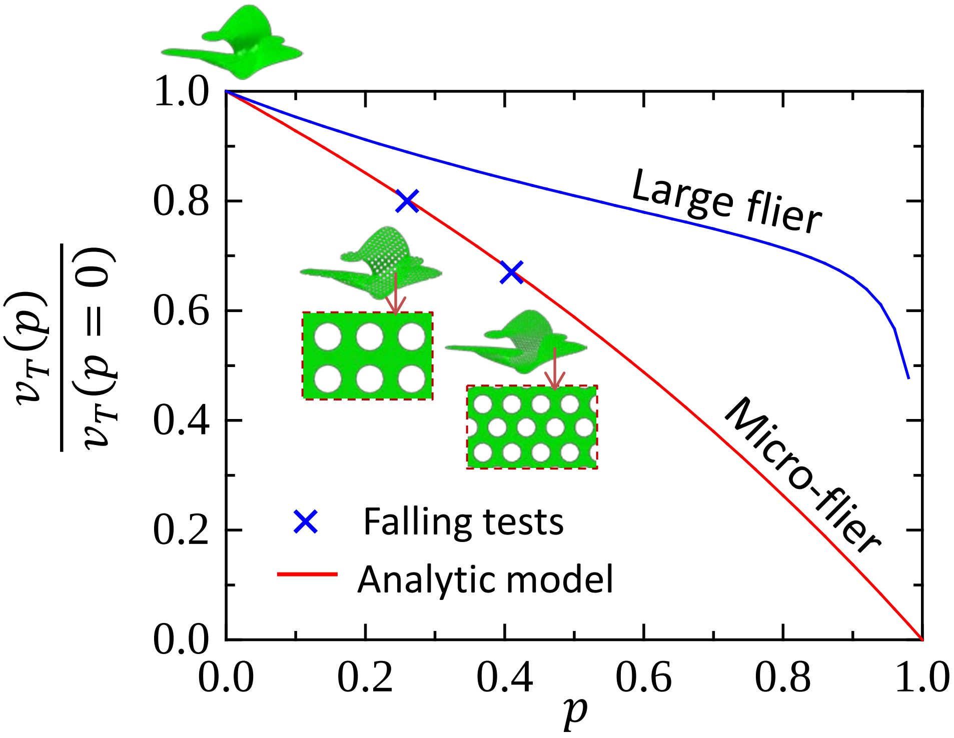

Figure S10. Terminal velocity versus porosity (p) for micro- and macro- scale fliers. The terminal velocity for the microflier is validated by experimental falling tests (Fig. 3b).

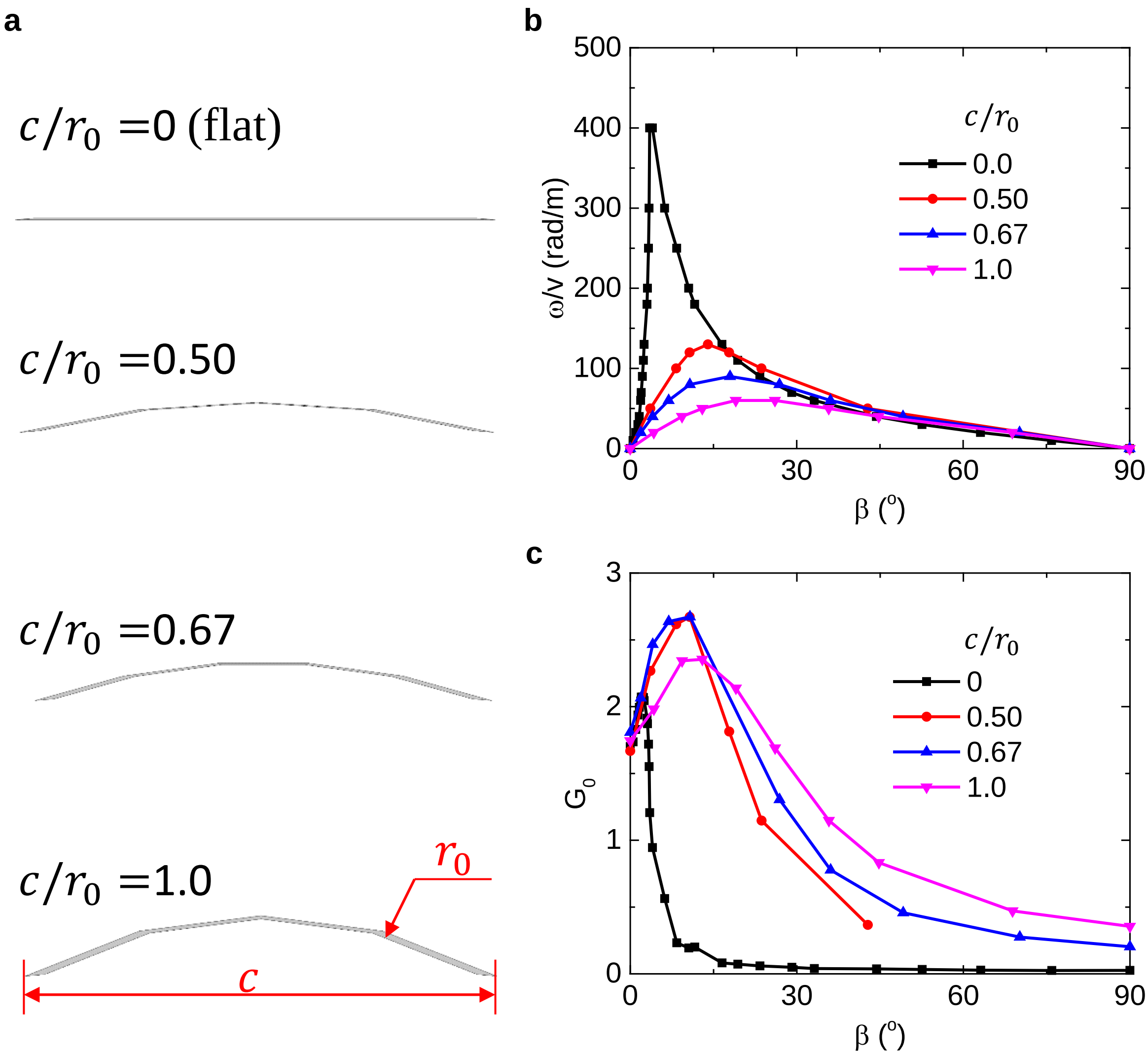

Figure S11. Effect of airfoil curvature for fliers at large Reynolds numbers. (a) Scheme of airfoil (cross section of a blade) with different curvatures. (b) ω/v_t and (c) G_0 versus blade tilt angle with different airfoil curvatures (from flat to curved), at large Reynolds numbers.

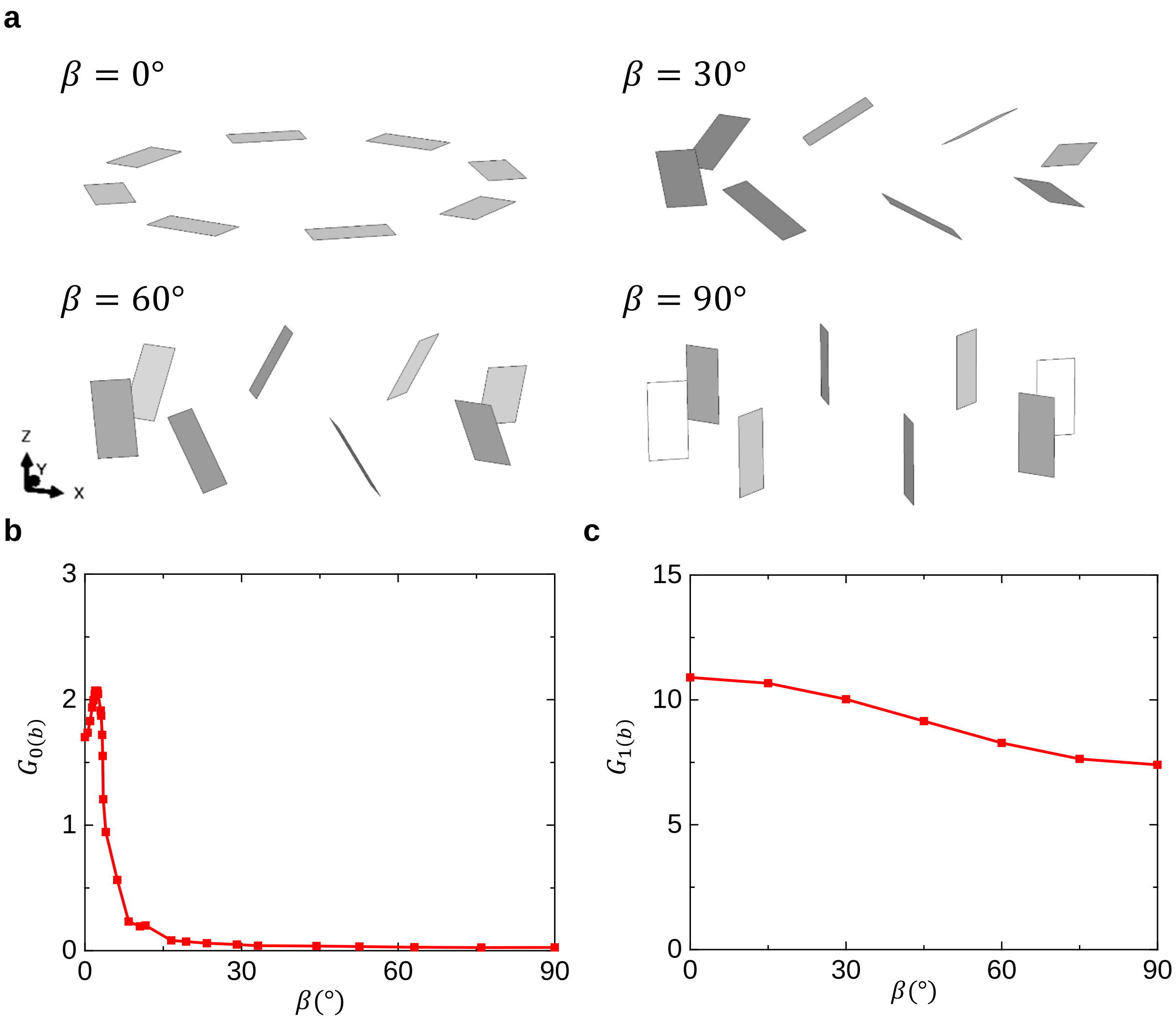

Figure S12. Effect of tilt angles of blades on G_0 and G_1. (a) Scheme of the simplified flier model with different tilt angles (β). The effect of tilt angle on (b) G_0 and (c) G_1.

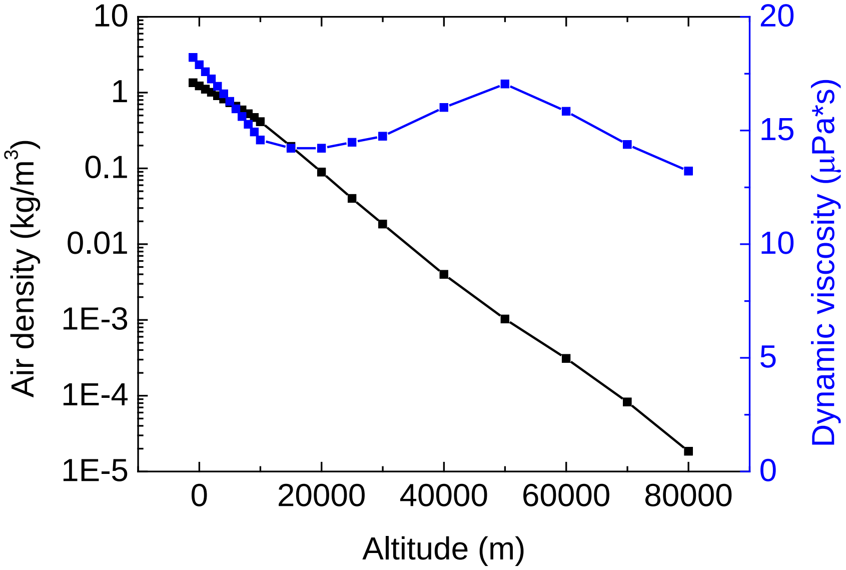

Figure S13. Effect of air properties. Air properties (density and dynamic viscosity) of US standard atmosphere at altitudes ranging from 0 to 80,000 m.

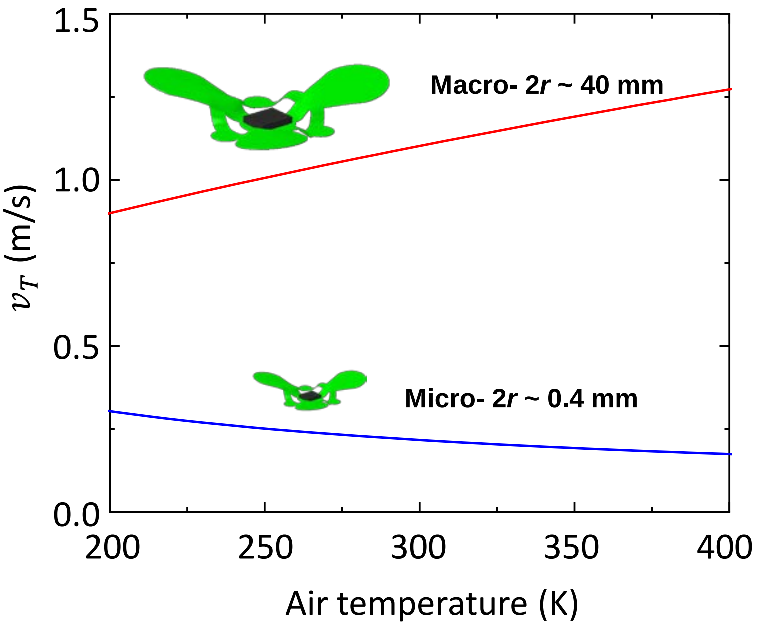

Figure S14. Effect of air properties. Effect of air temperature on terminal velocity.

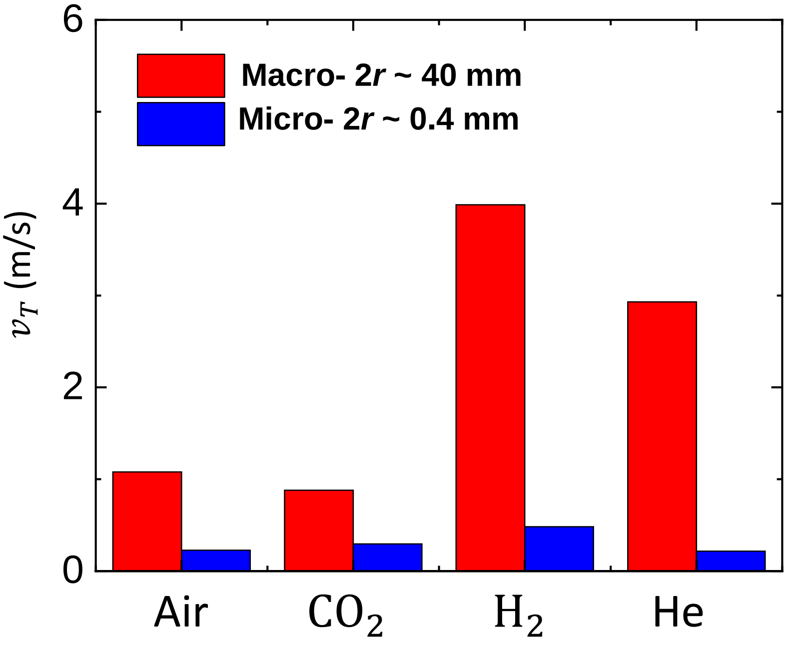

	Air	CO_2	H_2	He
$\rho(\mathrm{kg/m^3})$	1.225	1.842	0.0899	0.1664
$\mu(\mu Pa\cdot s)$	17.89	13.70	8.40	18.70

Figure S15. Effect of molecular makeup. Prediction of CFD for small and large fliers falling in different gases.

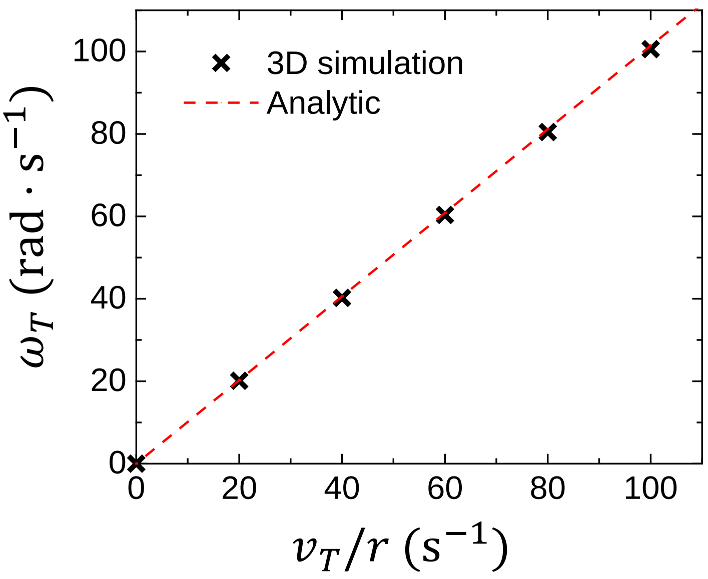

Figure S16. Scaling law for the terminal rotating speed of a flier. The rotating speed ω_T versus v_T/r, and the CFD results show a linear relationship, consistent with the analytic model.

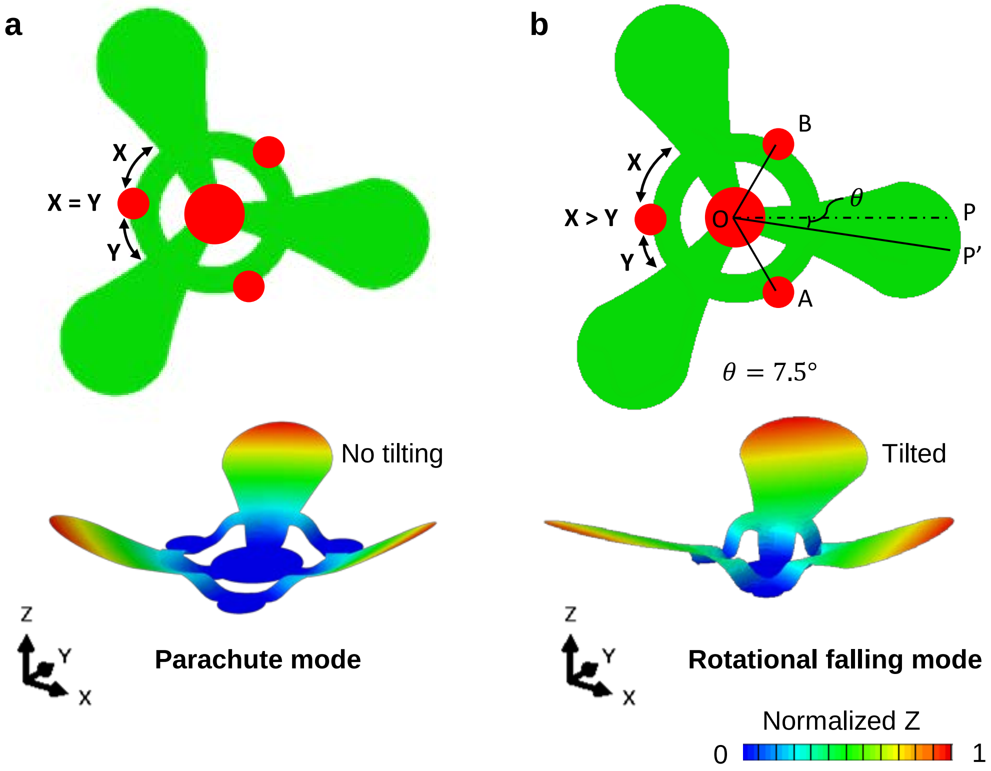

Figure S17. Mechanical simulation of a 3D microflier [3,H,0.75]. Schematic images of (a) a parachute design where the blades have no rotational tilting, and (b) a rotating flier design with rotationally tilted blades.

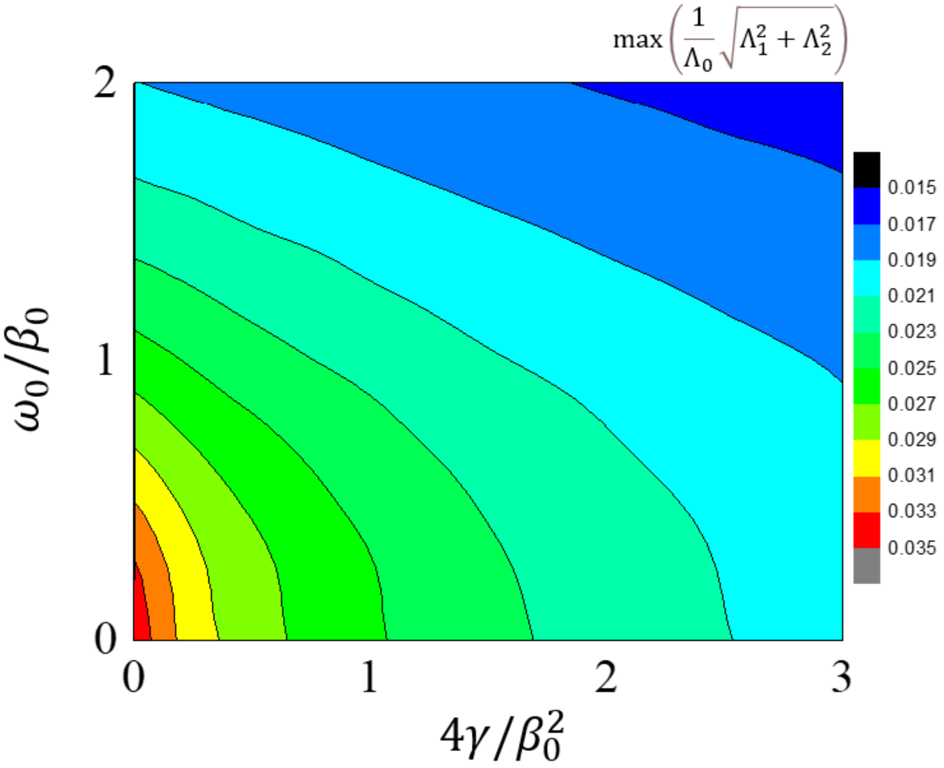

Figure S18. Maximum perturbed angle. $Max\left(\frac{1}{\Lambda_0}\sqrt{\Lambda_1^2+\Lambda_2^2}\right)$ versus ω_0/β_0 and $4\gamma/\beta_0^2$.

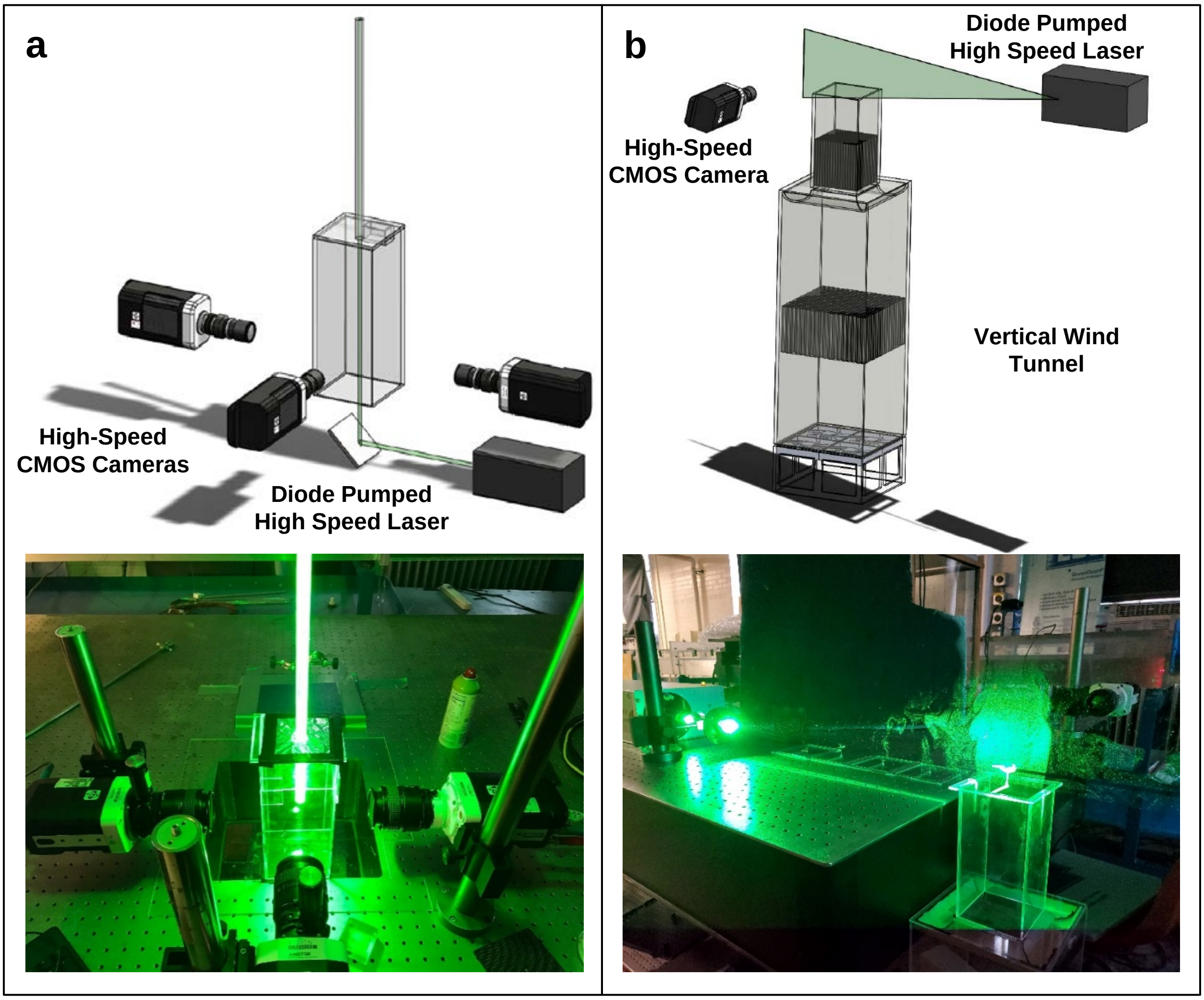

Figure S19. Experimental setups. (a) schematic (top) and photograph (bottom) of 3D-PTV experiment on free-falling mesofliers and (b) schematic (top) and photograph (bottom) of high speed PIV experiment on fixed 3D IoT fliers above a wind tunnel.

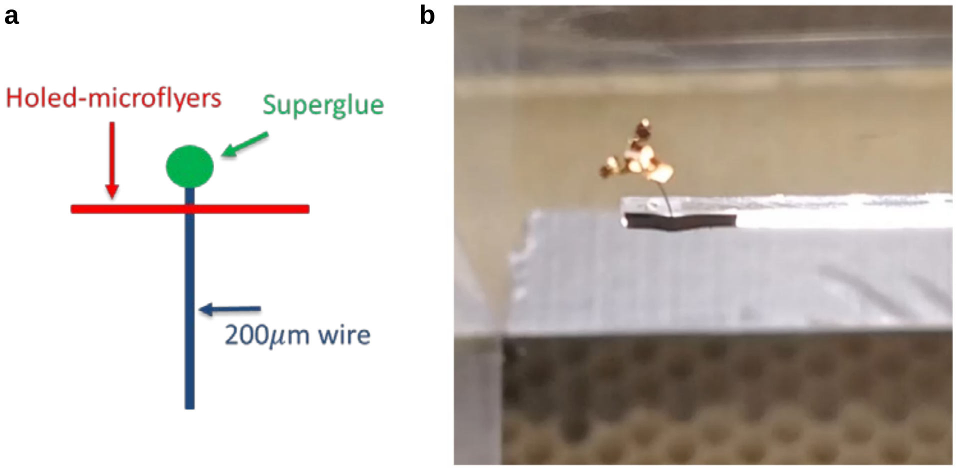

Figure S20. A fixed 3D macroflier above a wind tunnel. (a) Schematic diagram of a fixed macroflier, (b) video of comparing 2D (non-rotating) and 3D (rotating) macrofliers with $\mathrm{r} = 1.7$ mm.

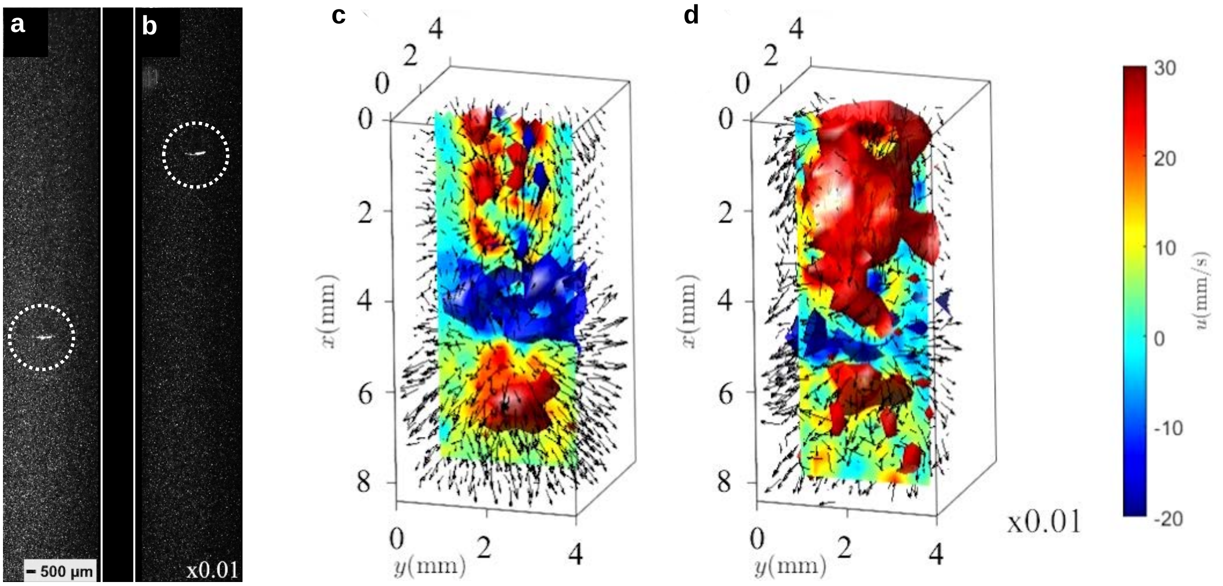

Figure S21. Free-falling a 2D precursor and 3D mesoflier. (a) Free-falling 2D precursor, (b) Free-falling 3D mesoflier. Instantaneous 3D flow velocity fields induced by free-falling (c) 2D precursor and (b) 3D mesooflier via 3D-PTV. The color denotes the in-plane 2D vertical velocity along the flier's center plane. Red and blue-sio-surfaces demonstrate iso-values of 15 and -5 mm/s, respectively.

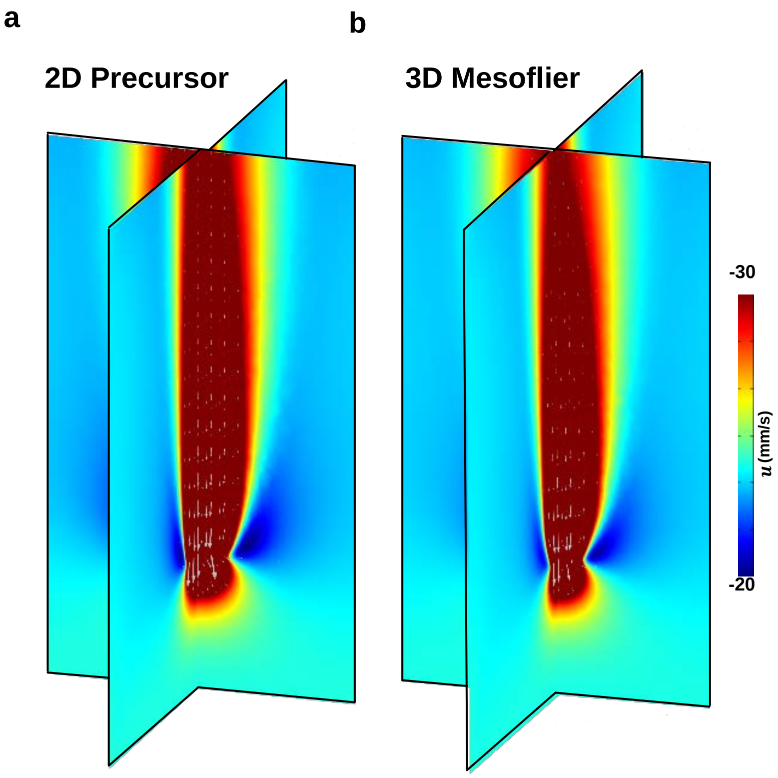

Figure S22. CFD simulated vertical flow field. (a) A 2D precursor and (b) 3D mesoflier [3,M,0.4] (Size scale 2r ~ 2 mm).

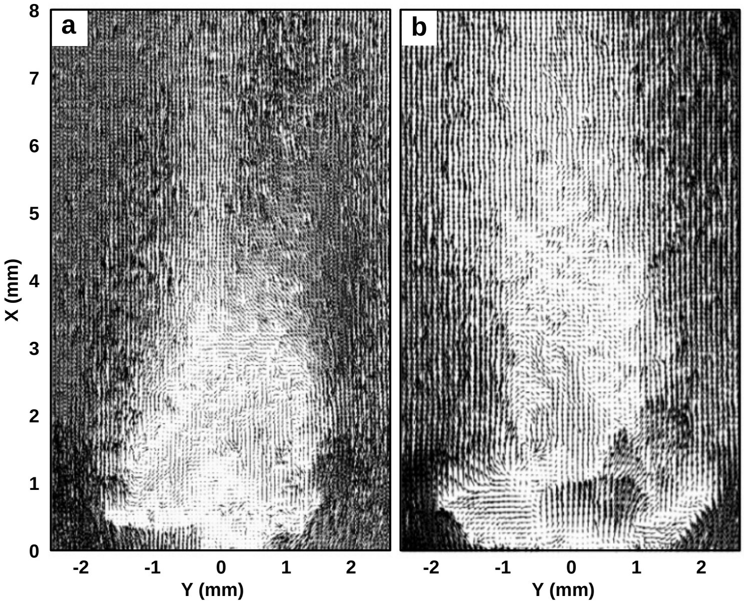

Figure S23. Experimental results for mesoflier. Instantaneous velocity fields induced by fixed (a) 2D precursor and (b) 3D mesoflier via PIV above the wind tunnel.

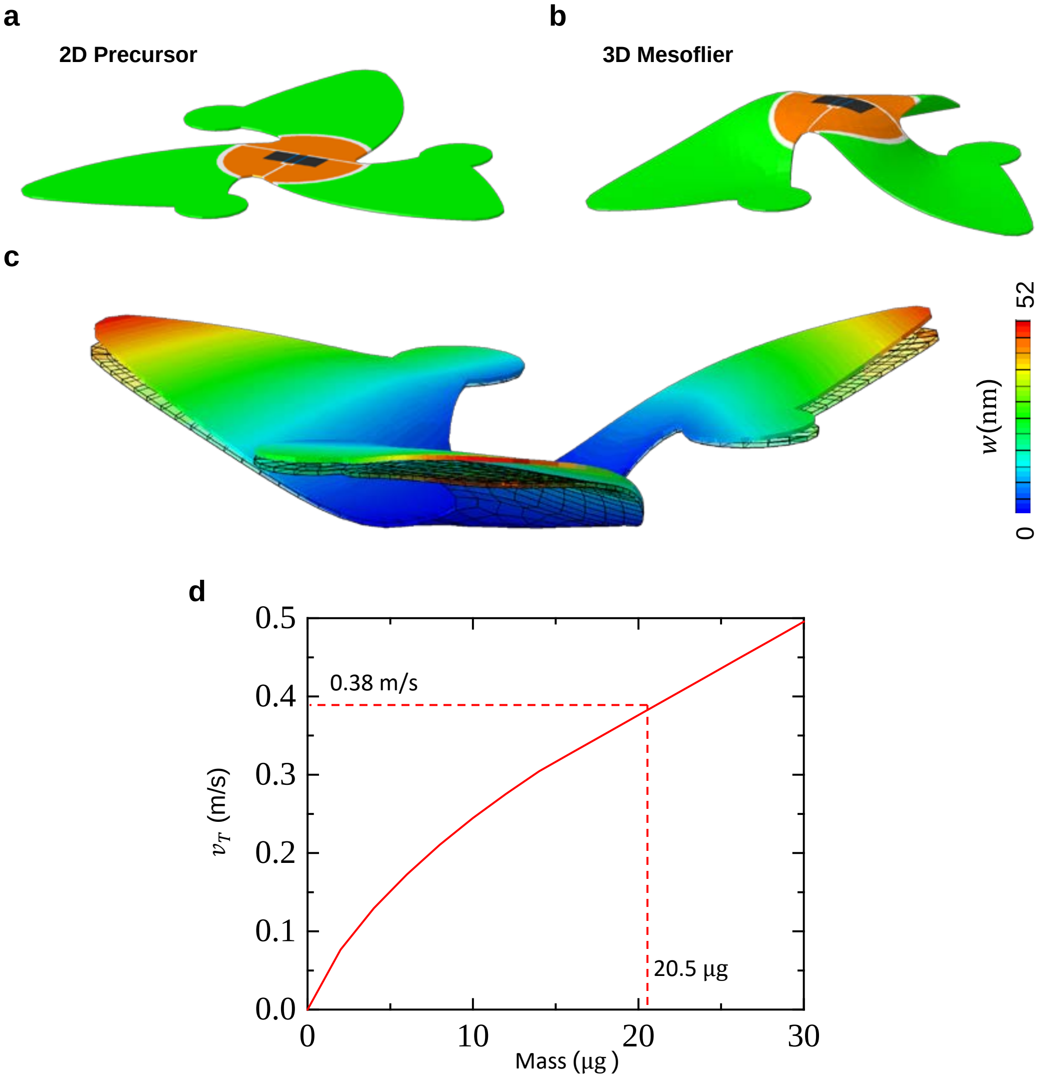

Figure S24. Simulations for 3D mesofliers with design I [3,M,0.4]. FEA showing (a) 2D precursor and (b) 3D configuration for the mesoflier. (c) Deflection of the 3D mesoflier during free-fall at the terminal velocity. The deflection is magnified by 1000 times. (d) CFD results for the terminal velocity as a function of the mass of the mesoflier.

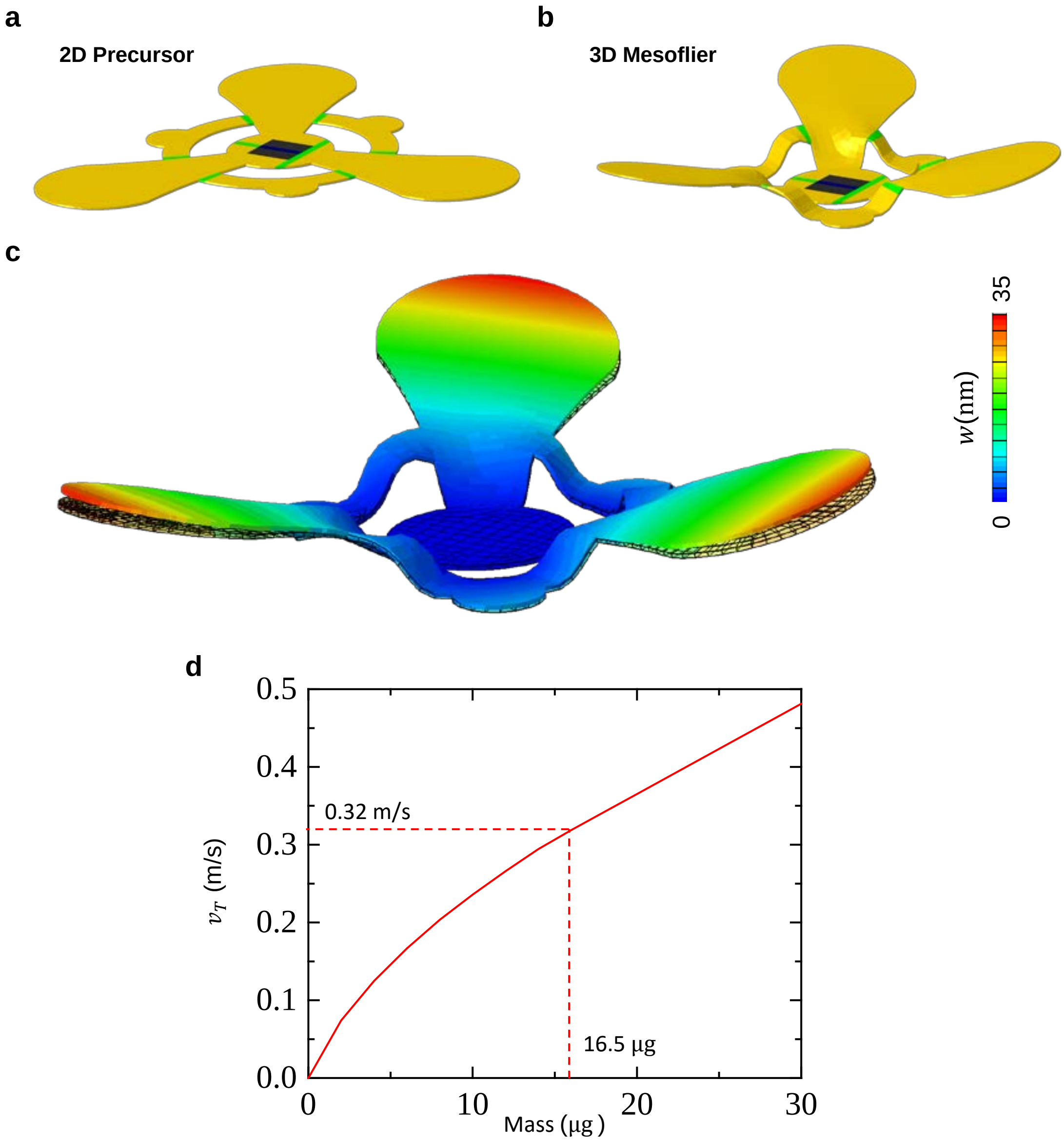

Figure S25. Simulations for 3D mesofliers with design II [3,H,0.75]. FEA showing (a) 2D precursor and (b) 3D configuration for the mesoflier. (c) Deflection of during free-falling at the terminal velocity. The deflection is magnified by 1000 times. (d) CFD results for the terminal velocity as a function of the mass of the mesoflier.

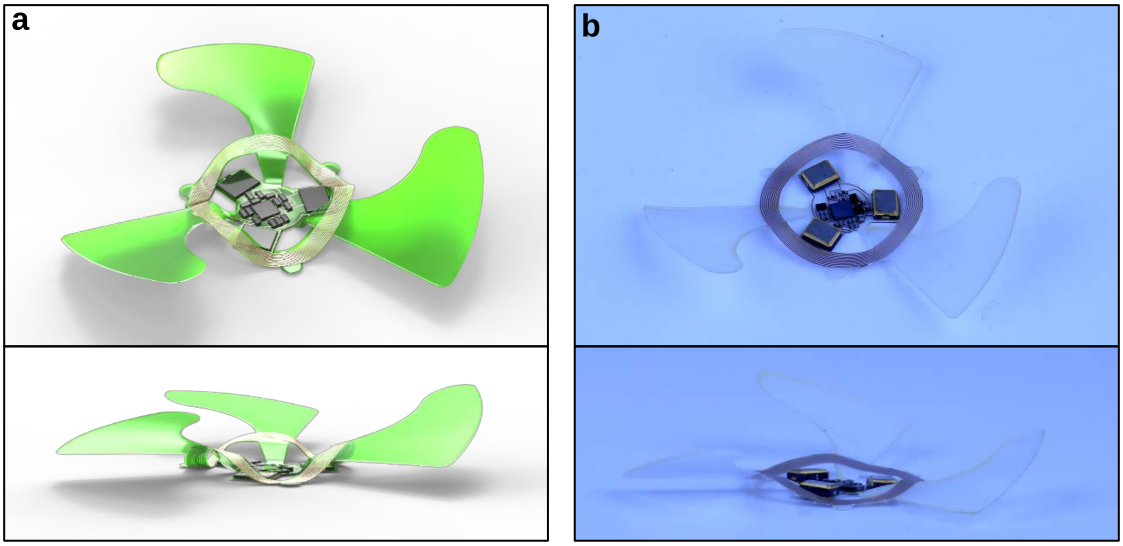

Figure S26. A 3D IoT macroflier with another design. (a) Mechanical simulation results and (b) photographs with a circuit to measure fine dust pollution through the light dosimetry method.

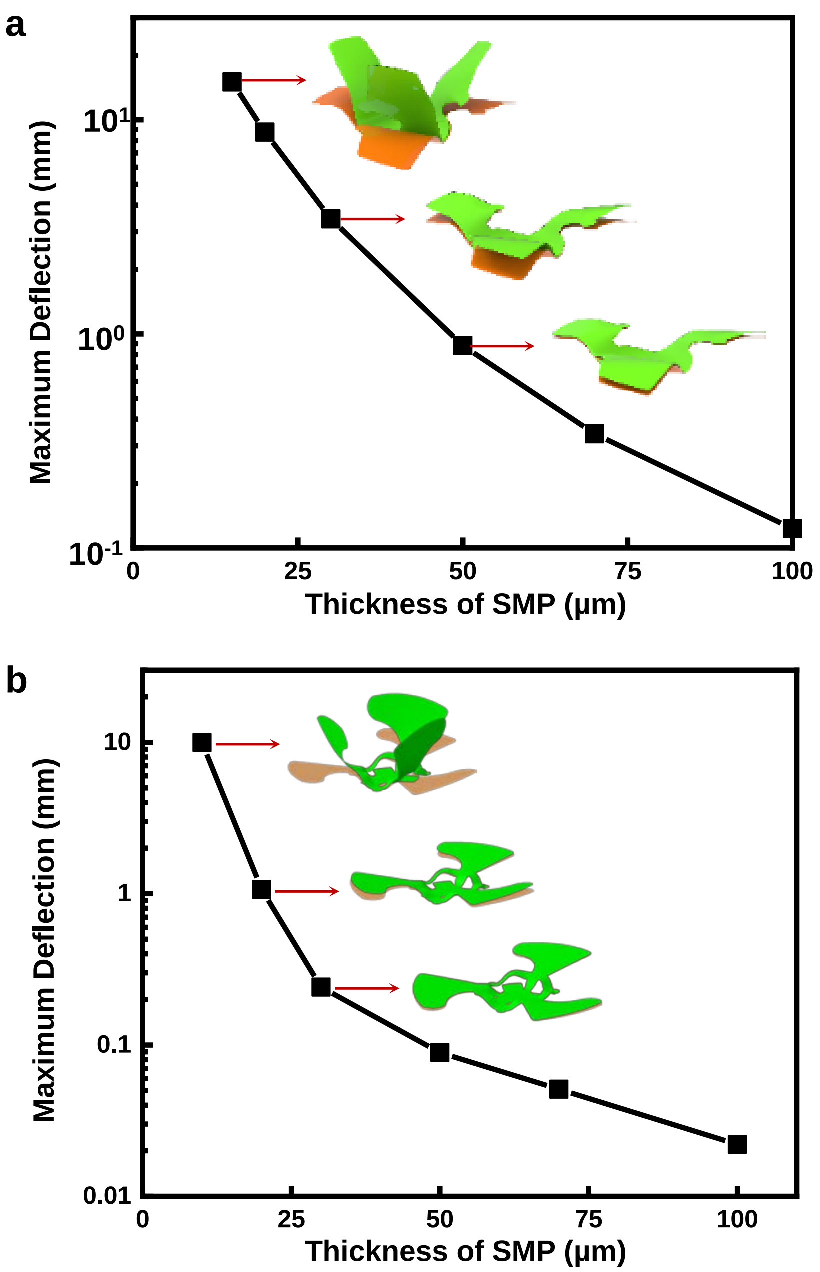

Figure S27. Effect of thickness on the deflection of 3D IoT macrofliers during falling. 3D IoT macrofliers with design of (a) Fig. 4e and (b) Fig. S24, respectively.

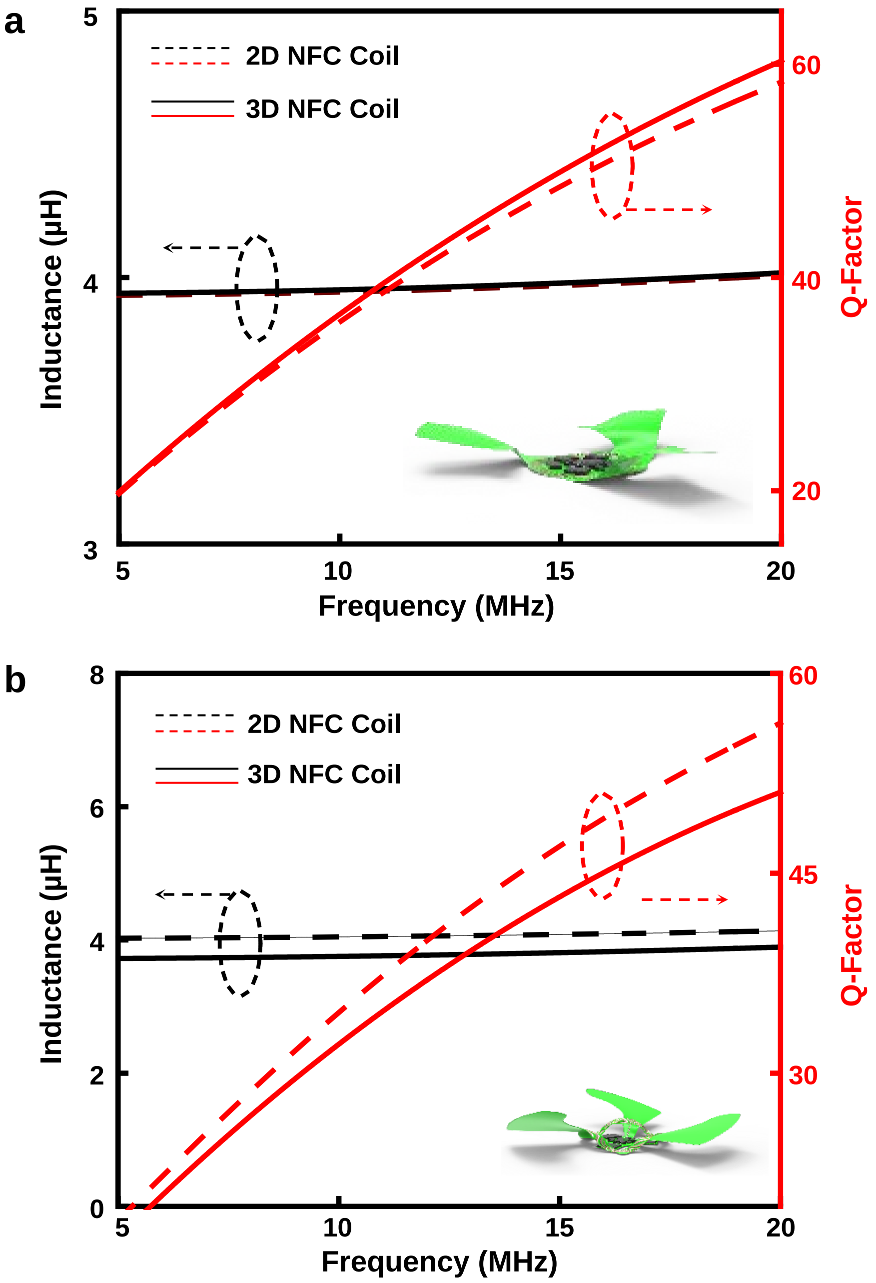

Figure S28. Electromagnetic simulations. Inductance and Q-factor for 3D IoT macrofliers with design of (a) Fig. 4e and (b) Fig. S24 for 2D/3D configuration, respectively.

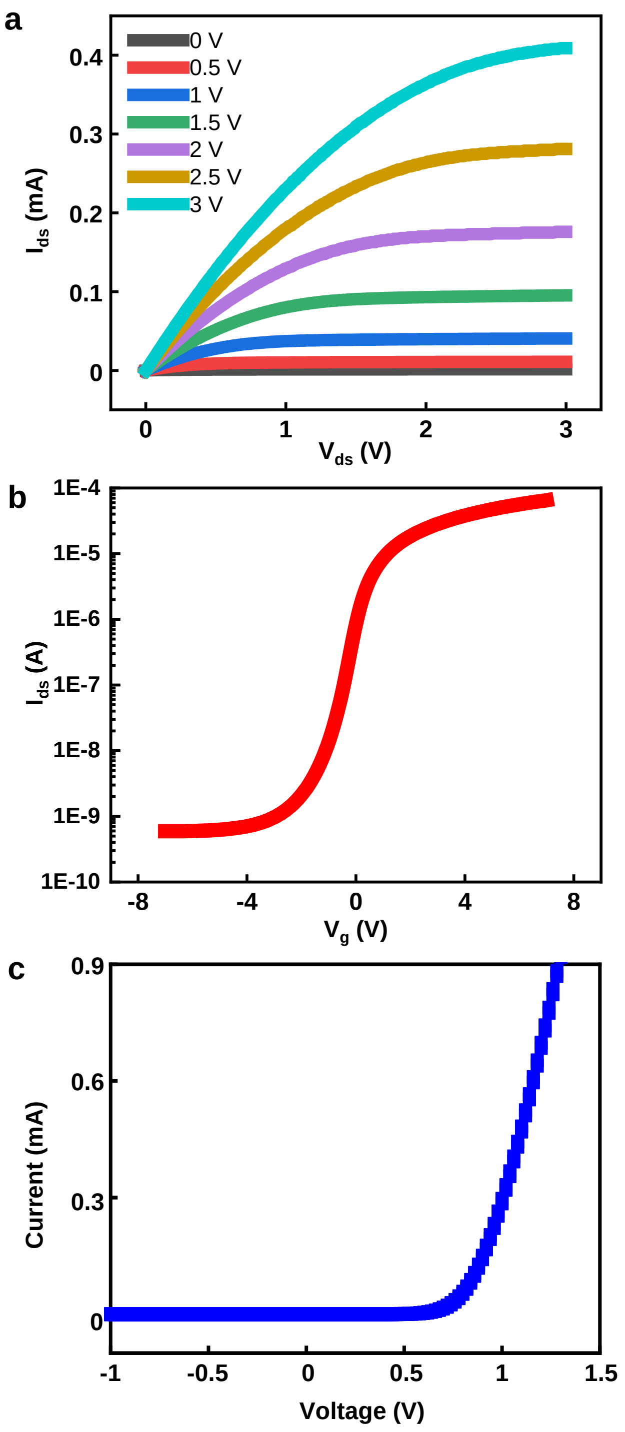

Figure S29. The electrical characteristics of silicon NM n-channel transistor (channel width/length = 80/20 μm) and diode integrated with 3D mesofliers. (a) Drain current as a function of source/drain voltage for the gate voltages from 0 to 3 V. (b) The log scale transfer curves as a function of gate voltage from -1 to 1.5 V. (c) Current-voltage characteristics of a diode.

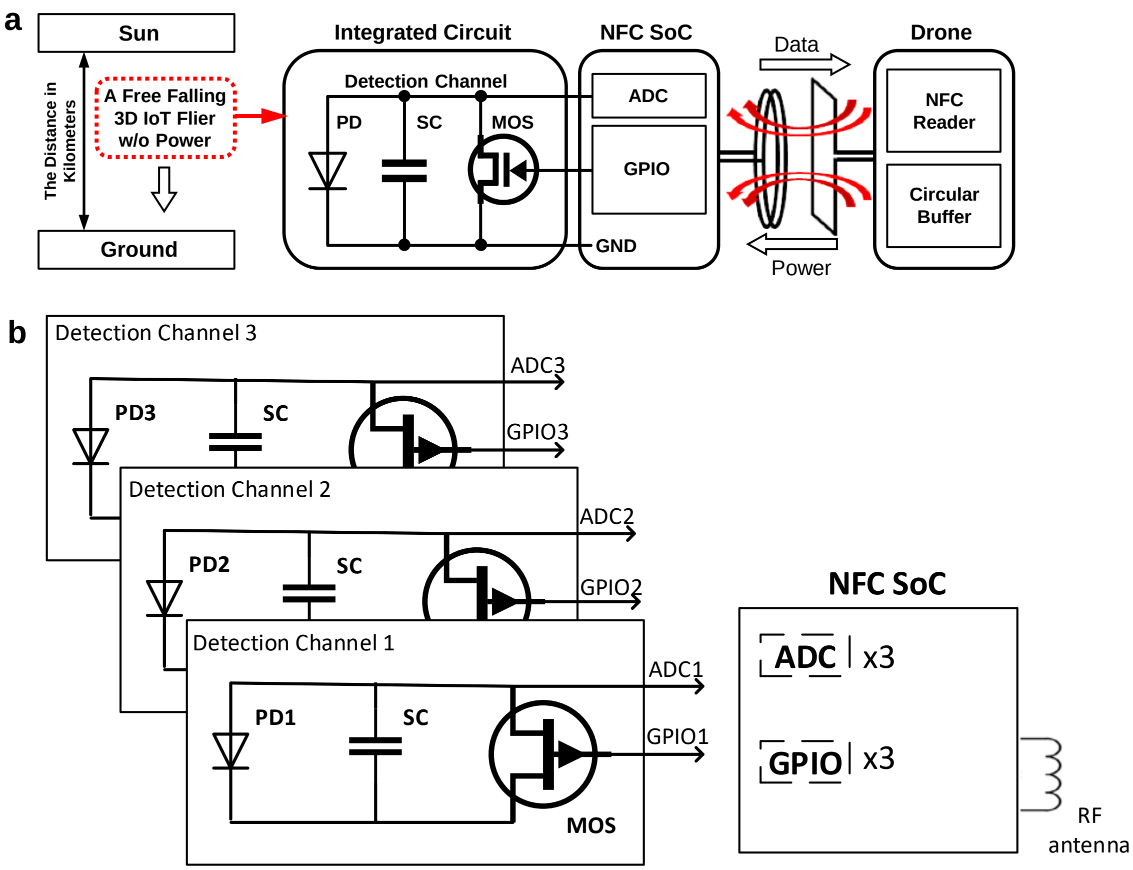

Figure S30. Circuit schematic of a battery-free, 3-channel dosimeter for fine dust monitoring. (a) A 3D IoT macroflier and its wireless interface to a drone. (b) Each detection channel consists of a photodiode (PD), a supercapacitor (SC), and a MOSFET (MOS). Upon light exposure, PD continuously generates photocurrent and SC passively stores the accumulated charge. The voltage bias of the SC read via ADC is proportional to the total exposure dose. Simultaneous dosimetry at up to three different wavelengths are possible by PD selection. An Near Field Communication System on Chip (NFC SoC) allows for a battery-free and wireless data transfer and power transmission. Wirelessly activated GPIO supplies 1.5V to the gate of the MOS and triggers SC discharge.

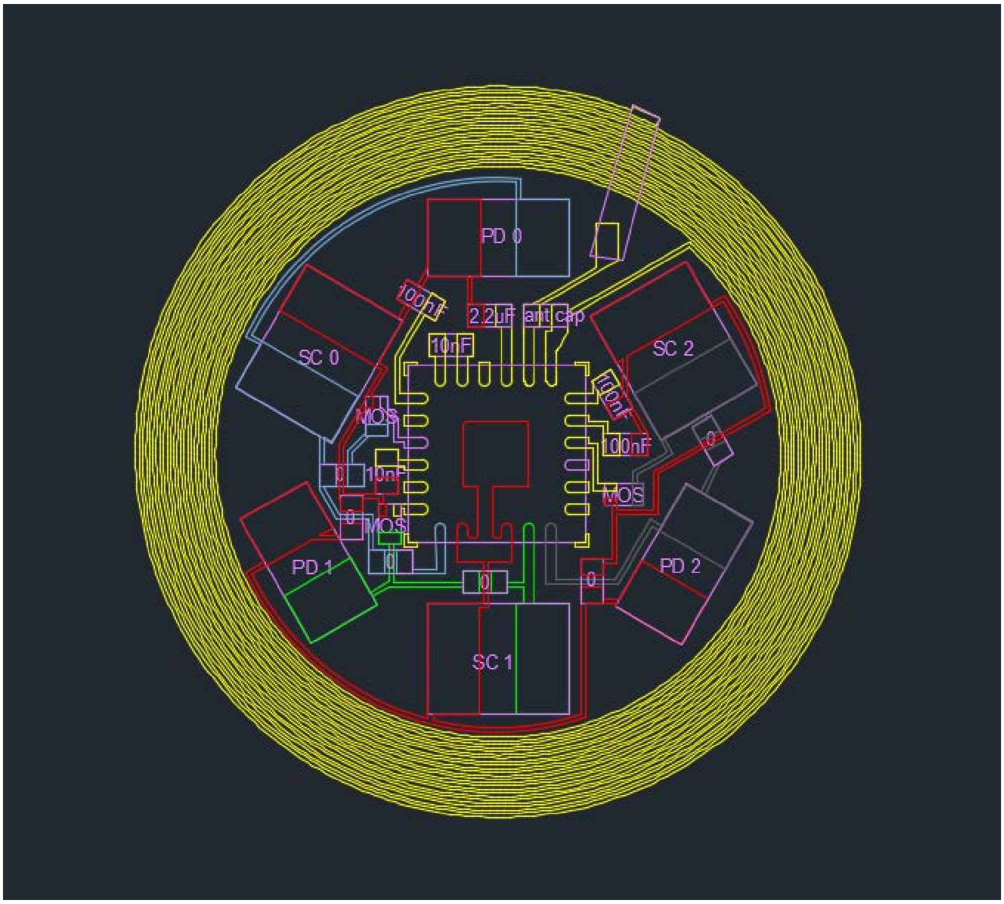

Figure S31. CAD design. Electronic components and metal interconnectors for a 3D IoT macroflier.

Table S1. Electronic components. The list of a detailed information of electronic circuits for a battery-free, 3-channel dosimeter for fine dust monitoring.

Item	Manufacturer	Catalog Number	Description
NFC Chip	Texas Instruments	RF430FRL152HCRGER	RFID Transponders Sensor Transponder
Photodiode	Advanced Photonix	PDB-CD160SM	Photodiode 850nm 20ns 120° 2-SMD, Gull Wing
MOSFET	Texas Instruments	CSD17381F4	MOSFET N-CH 30V 3.1A 0402
Super-Capacitor	Seiko Instruments	CPH3225A	CAP 11MF 3.3V SURFACE MOUNT
Capacitor 1	Murata Electronics North America	GRM033R60J225ME47D	CAP CER 2.2UF 6.3V X5R 0201
Capacitor 2	TDK Corporation	C0603X7R1A103K030BA	CAP CER 10000PF 10V X7R 0201
Capacitor 3	TDK Corporation	C0603X5R1A104K030BC	CAP CER 0.1UF 10V X5R 0201

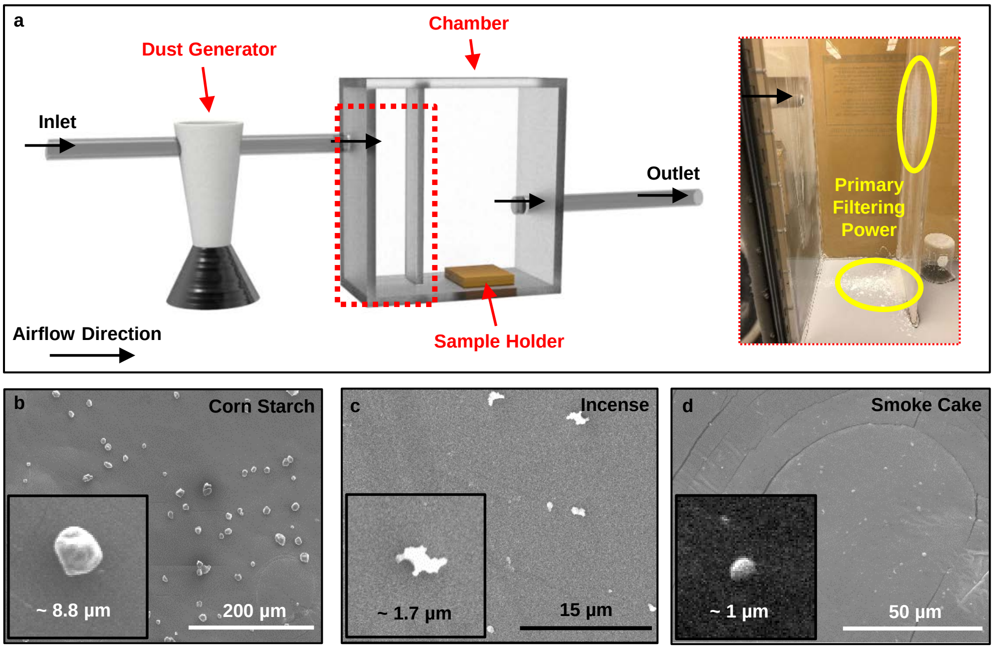

Figure S32. Experiments for particulate matter (PM). (a) A dust generation chamber operated with kitchen blenders. SEM images of fine dust generated by (b) corn starches, (c) incenses and (d) smoke cakes.

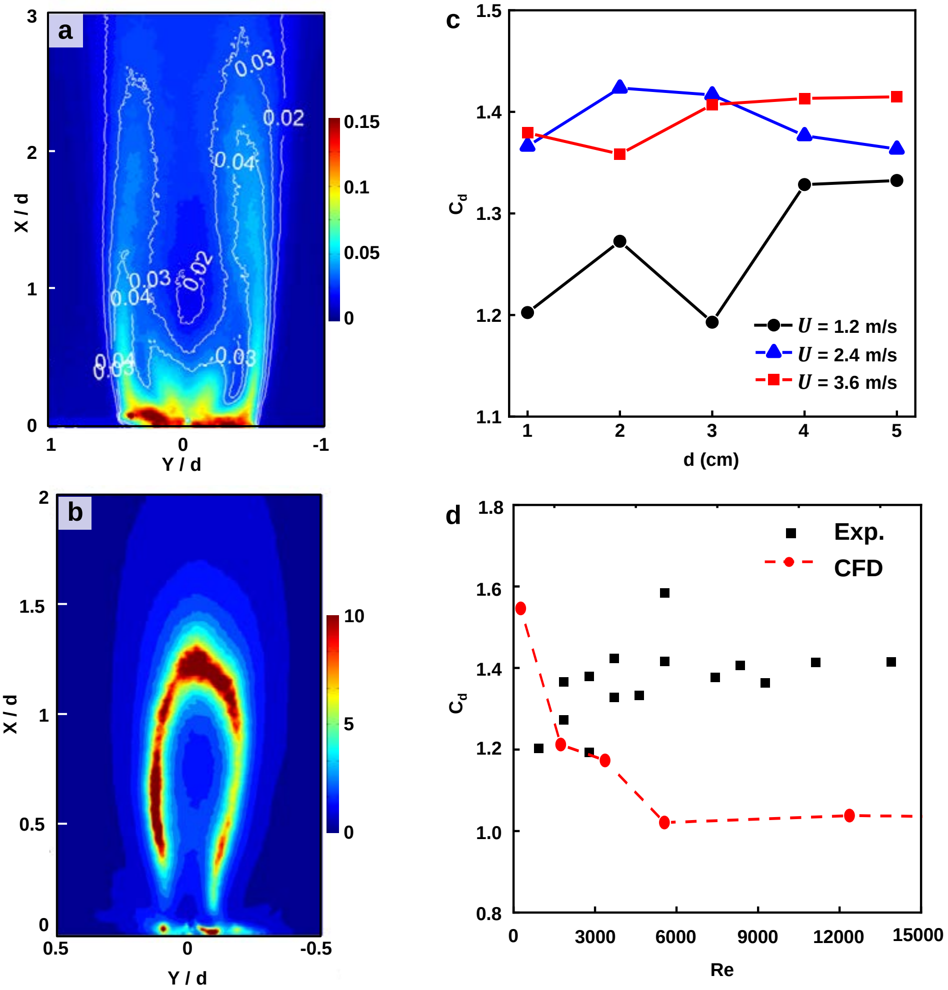

Figure S33. High-speed PIV measurements for 3D macrofliers. (a) turbulent Kinetic energy $TKE = \frac{1}{2}\left[\overline{(u')^2} + \overline{(v')^2}\right]/U^2$. (b) turbulence intensity $TI = \sqrt{\overline{(u')^2} + \overline{(v')^2}}/\sqrt{\bar{u}^2 + \bar{v}^2}$. (c) drag coefficient, C_d, calculated from velocity profiles vs diameters, d. (d) C_d vs Re.

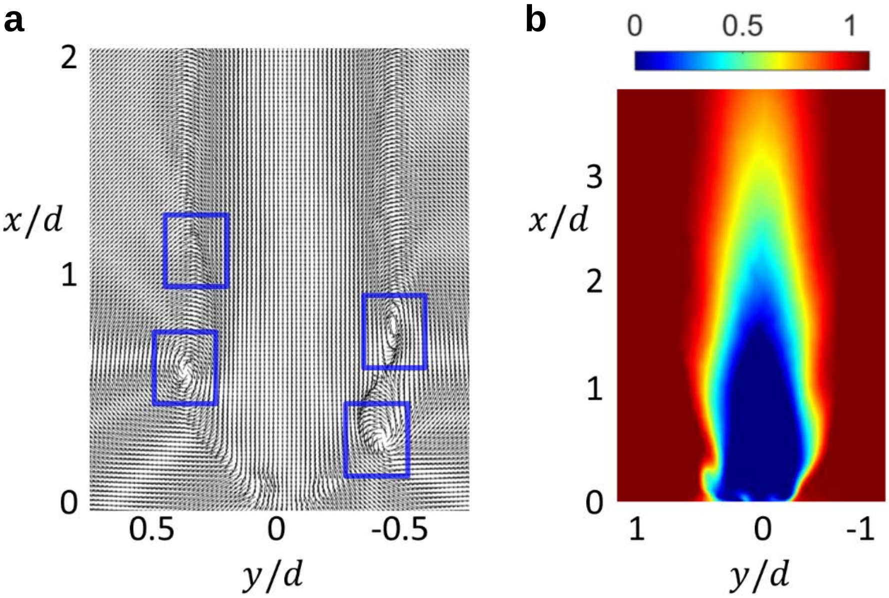

Figure S34. CFD results for a 3D IoT macroflier. (a) Instantaneous velocity field. (b) Mean velocity field in the streamwise direction u/U.

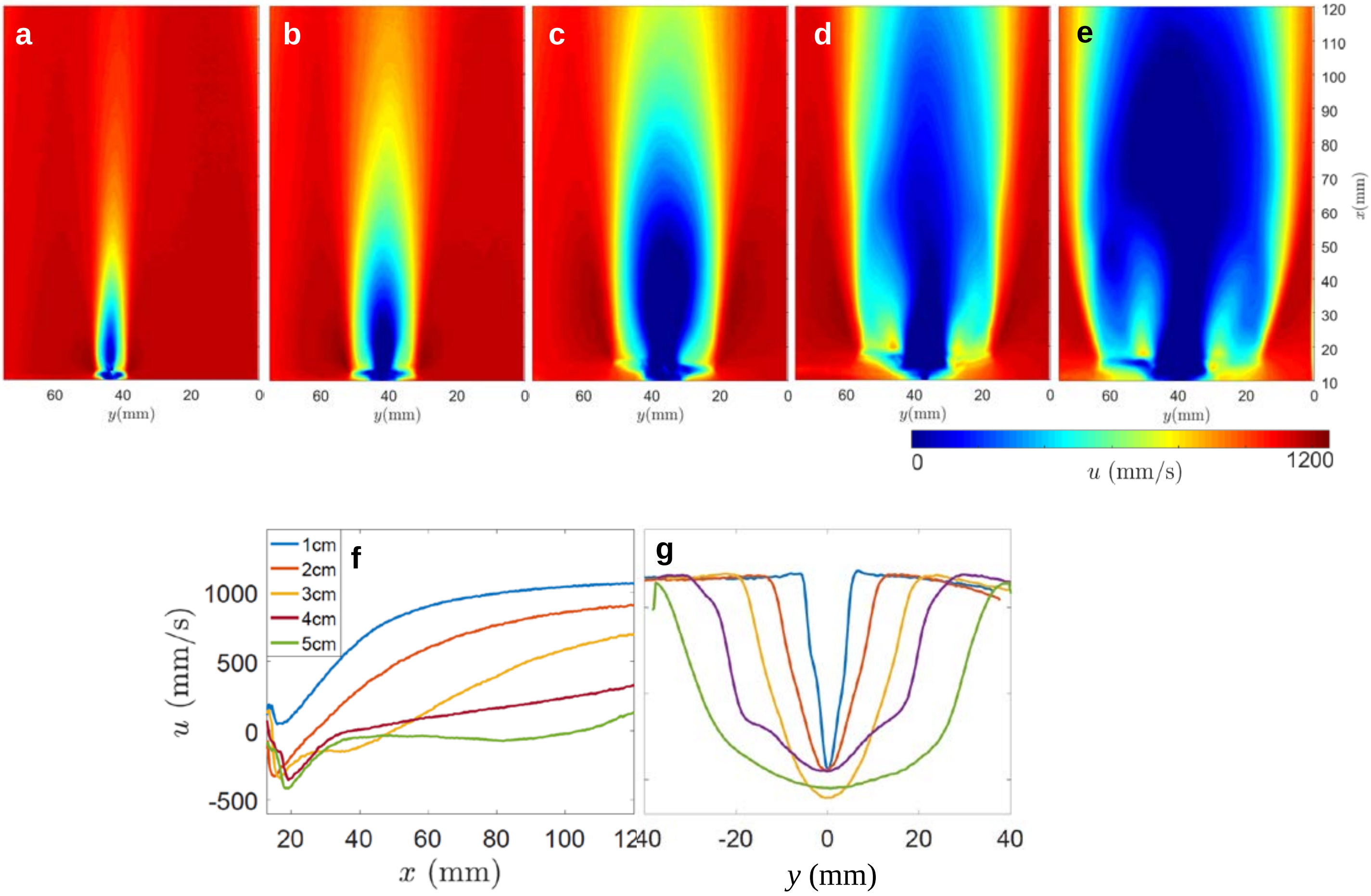

Figure S35. PIV results for 3D IoT macrofliers. Mean velocity field of (a) 1cm, (b) 2cm, (c) 3cm, (d) 4cm, and (e) 5 cm-diameter 3D IoT macrofliers at incoming velocity *U*=1.2m/s. Velocity profiles along the (f) center-axis and (g) spanwise direction at 12 diameter downstream.

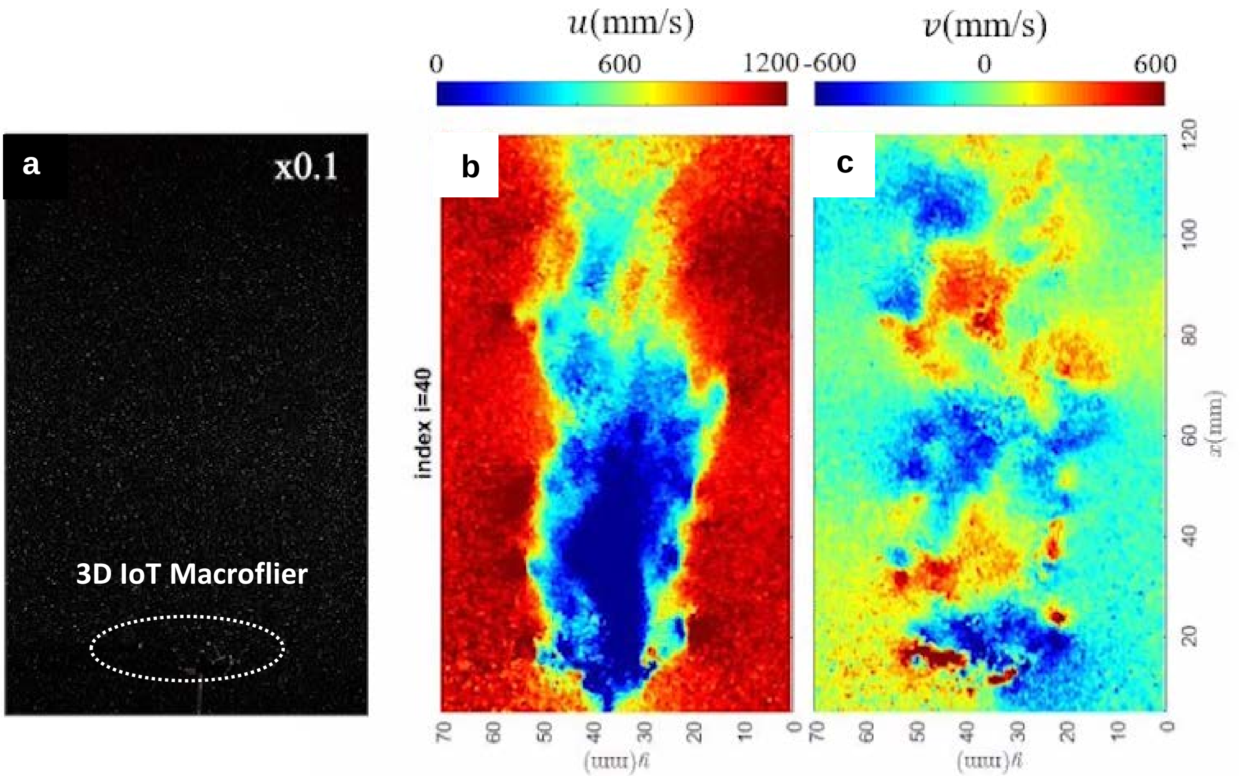

Figure S36. High-speed PIV flow measurements for 3D IoT macrofliers. (a) raw image sequence, (b) vertical velocity field, and (c) horizontal velocity field.